

## **Synthesis of Low-loss Single-crystalline Silver Films for Quantum Nanophotonics**

*Ilya A. Rodionov\**, Aleksandr S. Baburin, Alexey P. Vinogradov, Aidar R. Gabidullin, Sergey S. Maklakov, Swen Peters, Ilya A. Ryzhikov, and Alexander V. Andriyash

A. S. Baburin, A. R. Gabidullin, Prof. I. A. Rodionov, Dr. I. A. Ryzhikov

Research and Educational Center Functional Micro/Nanosystems, Bauman Moscow State Technical University, 105005 Moscow, Russian Federation

E-mail: irodionov@bmstu.ru

Dr. I. A. Rodionov, A. S. Baburin, Dr. A. P. Vinogradov, A. R. Gabidullin, Dr. A. V. Andriyash

Dukhov Research Institute of Automatics, 127055, Moscow, Russian Federation

S. Peters

SENTECH Instruments GmbH, 12489, Berlin, Germany

Dr. A. P. Vinogradov, Dr. S. S. Maklakov, Dr. I. A. Ryzhikov

Institute for Theoretical and Applied Electromagnetics RAS, 125412, Moscow, Russian Federation

Keywords: single-crystalline; silver film; atomically flat; low-loss; quantum nanophotonics, plasmonics

Different optoelectronic devices have been discussed recently,<sup>[1-10]</sup> and these devices are based on the possibility of controlling and concentrating light using surface plasmon polaritons (SPPs), which are hybrid photon-electron waves, localized into a sub-wavelength volume and propagated along the interface of two materials with different dielectric functions. SPPs are still considered an attractive tool to achieve extreme light confinement for practical applications, such as subwavelength waveguides,<sup>[2]</sup> low-threshold continuous-wave operation nanolasers and single-photon quantum emitters,<sup>[3-5]</sup> new ultra-sensitive applications in biosensing and environmental

sensing,<sup>[6]</sup> photon-plasmon and plasmon-photon modulators,<sup>[7]</sup> photovoltaics,<sup>[8]</sup> and metamaterials.<sup>[9]</sup> The effective combination of the low-loss substrate-metal system and nanostructure patterning techniques have to be found, as the brilliant initial metal optical properties can be dramatically degraded during device fabrication.

Silver (Ag) is by far potentially the most preferred plasmonic material because it has the lowest optical losses among all the metals and the longest SPP propagation length at optical and near-IR frequencies;<sup>[11-16]</sup> these properties are even superior to graphene.<sup>[12]</sup> However, silver is one of the most challenging metals for sub-50-nm-thick single-crystalline growth because of its natural chemical instability and high reactivity,<sup>[17]</sup> as well as its high sensitivity to substrate surface reconstruction and impurities, lattice-matched substrate dewetting at elevated growth temperatures<sup>[18]</sup> and degradation of optical properties over time.<sup>[12]</sup> Over the last decades, a few works have reported the preparation of single-crystalline silver films using high vacuum physical vapor deposition (PVD)<sup>[14,19]</sup> techniques and ultra-high vacuum (UHV) molecular beam epitaxy (MBE).<sup>[15,19,20]</sup> However, the experimentally measured optical and plasmonic properties of these films are still far from the phenomenal theoretically predicted values. To boost the plasmonic device performance, a patterning-compatible technology for the deposition of low-loss sub-50 nm continuous ultra-flat single-crystalline silver films must be developed.<sup>[5,14-16]</sup>

In this work, we first present the PVD technology for sub-50 nm single-crystalline silver film growth with an atomically smooth surface, which is the result of a detailed study on the growth mechanism and a scrupulous analysis of more than 2000 samples.<sup>[21-23]</sup> No adhesion layers are required for this process, and it is reproducible under standard cleanroom conditions. The proposed two-step film growth mechanism is fundamentally different from the previously reported PVD methods<sup>[14,24]</sup> in which the process is defined only by the temperature (the energy of atomic clusters coming to the substrate) and the deposition rate (the number of atomic clusters coming to the

substrate per unit time),<sup>[5,15,19]</sup> as well as from the expensive UHV MBE methods. In the first step, an «ideal» seed consisting of atomically flat top two-dimensional (AFT 2D) islands is deposited on the substrate under elevated temperatures (**Figure 1**). In the second step, the deposition is stopped, and the substrate is cooled to room temperature in the same vacuum cycle. At room temperature, more silver is deposited on the AFT 2D seed until a continuous film is formed. Upon subsequent annealing at a temperature higher than the first-step temperature, the crystalline structure and surface roughness are improved, and this is accompanied by a reduction in the growth defect density. This process could be used for various metal-substrate systems, as demonstrated by tests involving the evaporation of sub-50 nm single-crystalline gold and aluminum films (the results will be published later). We believe that the dramatic improvement in the film characteristics relies on the combination of two mixed evaporation modes that are partially controlled by quantum size effects (QSEs). Considering this dual-phase experimental nature as well as the improved film parameters, this deposition process was named the «SCULL» (Single-crystalline Continuous Ultra-flat Low-loss Low-cost) process.

This study focuses on the metal-on-substrate systems of Ag on Si(111), Ag on Si(100), Ag on Si(110), and Ag on Mica, which are normally susceptible to three-dimensional island growth at ultra-low thicknesses leading to subsequent film imperfections. Silicon and mica were chosen because they are well-known lattice-matched substrates for silver epitaxial growth and are widely used in various applications. Using the SCULL process, 35 to 100-nm-thick single-crystalline silver films were evaporated (base pressure  $3 \times 10^{-8}$  Torr, see the Supporting Information for details) on different substrates (**Table 1**). All the deposited films were continuous, without voids and pits, and had an atomically smooth surface with an area of over  $15 \times 15 \text{ mm}^2$ .

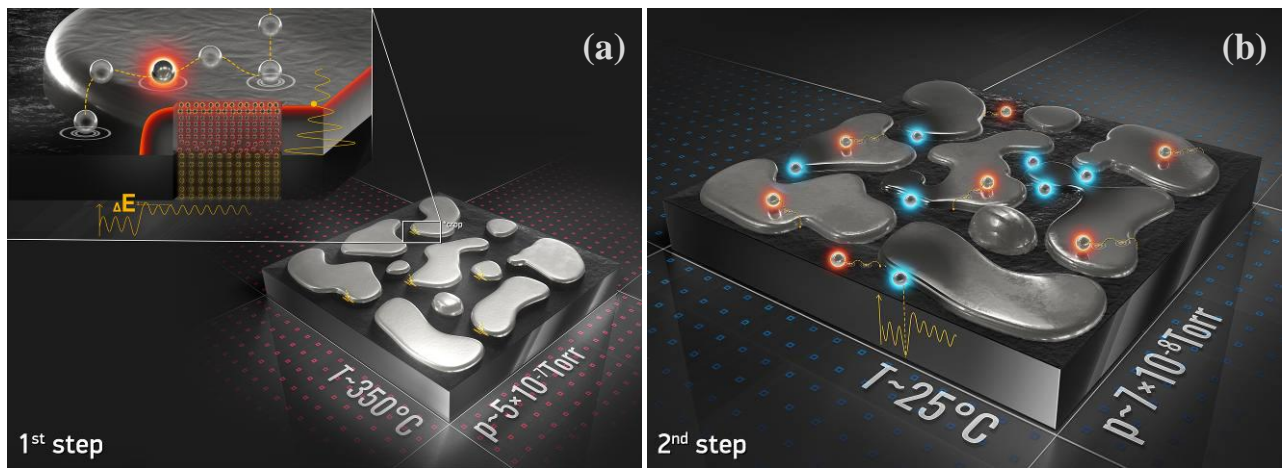


**Figure 1.** SCULL technology two-step silver film growth. In the first step, under elevated temperatures of 280-420 °C, a 1 to 25-nm-thick AFT 2D seed layer undergoes self-controlled growth by quantum size effects. In the second step, in the same vacuum cycle, the deposition stops, the substrate is cooled to room temperature, and a continuous silver film is formed in the 2D growth mode.

Consider the specific example of using the SCULL process for Ag(111) thin film growth on a Si(111) substrate. In the growth first step, more than 70% of all the growing islands must be AFT 2D Ag(111) islands (**Figure 2**) with three key features: firstly, the thickness of the islands is much less than the effective average island size; secondly, the self-controlled island thickness and crystalline structure over a large area; and thirdly, an internal stress-induced energy accumulation in the islands. The 2D islands preferentially form under the Frank-van der Merwe growth mode, which is also known as layer-by-layer 2D growth.<sup>[25]</sup> The growth mechanism and Ag–Si(111) system conditions are determined by the substrate temperature, deposition rate and layer thickness.<sup>[26-28]</sup> We experimentally determined the temperature range (280-420 °C), deposition rate (0.5-10 Å/s) and thickness (1-25 nm) that enable AFT 2D Ag(111) island growth. An electronic growth (EG) model<sup>[29]</sup> based on the QSE could be used to explain the three key features of the AFT 2D islands. According to the EG model, growing AFT 2D Ag(111) islands are considered as an electron gas, which is confined to a 2D quantum well (QW) that is as wide as the thickness of the silver

islands.<sup>[30,31]</sup> The energy oscillates as a function of the island thickness (QW width), resulting in island thickness quantization (Figure 1a). At larger thicknesses (after an inter-mixing layer), the oscillation magnitude decreases, and it coincides with the Fermi energy for a bulk silver crystal. Above this thickness, the top silver layers of the islands grow under a homoepitaxial regime in the presence of these small energy oscillations, resulting in a quantized island thickness preference.<sup>[27,29,32]</sup> This enables the formation of an ideal seed layer on non-ideally lattice-matched substrates, even using standard deposition tools and under process parameter deviations. After the first step, the AFT 2D islands wet the substrate very well (Figure 2), and they have an irregular form with an average size ranging from 100-250 nm with an island-to-island distance of 2-50 nm.

**Table 1.** Thickness, surface roughness and microstructure of SCULL evaporated Ag films as a function of substrate type. AFM RMS roughness was determined from scans over a  $2.5 \times 2.5 \mu\text{m}^2$  area. SP RMS roughness was determined from scans over a 20- $\mu\text{m}$  length.

Substrate	Measured thickness [nm]	Crystalline structure	Rocking curve Ag peak, FWHM [°]	AFM RMS roughness [nm]	SP RMS roughness [nm]	Sample
Si (111)	35	Single-crystalline	0.325	0.09	0.71	S1
Si (100)	35	Single-crystalline	0.829	0.28	0.82	S2
Si (110)	35	Single-crystalline	0.831	0.37	0.69	S3
Si (111)	65	Single-crystalline	0.221	0.36	0.82	S4
Si (100)	65	Single-crystalline	0.400	0.28	0.74	S5
Si (110)	65	Single-crystalline	0.620	0.40	0.84	S6
Si (111)	100	Single-crystalline	0.368	0.43	0.90	S7
Mica	35	Single-crystalline	not measured	0.35	0.44	M1

We experimentally demonstrated (not shown) that as the thickness of the AFT 2D Si(111) seed layer increased, the two-dimensional growth became three-dimensional, resulting in the formation of a discontinuous film in the next process step. Note that the AFT 2D seed thickness was maximized, which provided nearly dislocation-free crystalline lattice growth of the Ag(111) island as well as the ultimate initial stress accumulation in the islands due to strained growth under high temperatures. Strained growth is induced by the onset of a screw dislocation influence and spiral growth. Both factors play an important role in the process described herein. The presence of a screw dislocation and spiral growth limits the maximum thickness of the ideal AFT 2D seed layer, with a

value of approximately 30-60 monolayers:<sup>[26]</sup> thus, the optimal thickness can be experimentally defined for each metal.

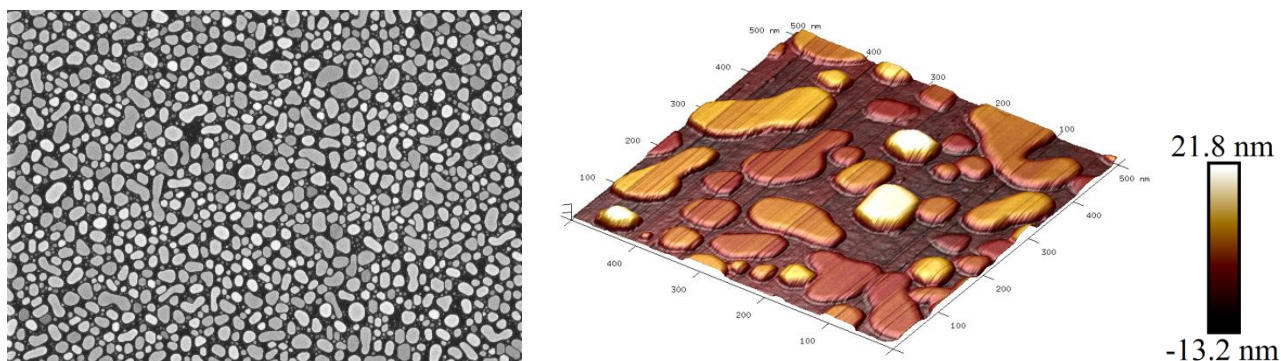


**Figure 2.** SEM image and  $0.5 \times 0.5 \mu\text{m}^2$  area AFM scan of AFT 2D Ag(111) islands deposited on a Si(111) substrate. Most of the AFT 2D Ag(111) islands are atomically flat with an RMS surface roughness value less than 50 pm.

At the second step, evaporation is stopped, and the substrate is cooled to room temperature. Then, silver is deposited at a deposition rate of  $0.5\text{-}5 \text{ \AA/s}$  on the AFT 2D seed (**Figure 3a**) until a continuous single-crystalline film is formed (Figure 3d). During the second step, almost all new adatoms coming to the substrate are adsorbed on the perimeter edge of the AFT 2D islands, eventually coalescing the islands with each other, thus completing the single-crystalline film. This growth mechanism is enabled by switching to the Stranovsky-Krastanov growth mode, which results in the spreading of dominant Ag(111) 2D islands due to a reduction in the Ag adatom surface diffusion length<sup>[33]</sup> and the generation of perfect crystalline lattice at the expense of energy relaxation, which was accumulated in the islands during the first step.<sup>[31,33]</sup> This is an important feature of the SCULL process: Ag adatoms hop along the atomically flat top surfaces of the 2D islands with almost no energy dissipation. At room temperature, the surface diffusion length of the Ag adatoms becomes comparable to the average size of the 2D islands, and the adatoms relax at the island perimeter (Figure 1b). Ag adatoms overcome the potential barrier on the edges (Figure 1a) via the intrinsic energy and stress relaxation accumulated in the islands. Consequently, a number of

desirable silver film transformations occur during the second step: firstly, the stress that was accumulated in the first growing step relaxes primarily into interactions with adatoms on the island edges, thus improving the crystalline structure of the AFT 2D islands. Secondly, almost all the incoming adatoms are absorbed on the AFT 2D island edges, resulting in a fully continuous silver film, even at a 10-20-nm thickness, ultimately resulting in a continuous film with a dominant Ag(111) orientation.

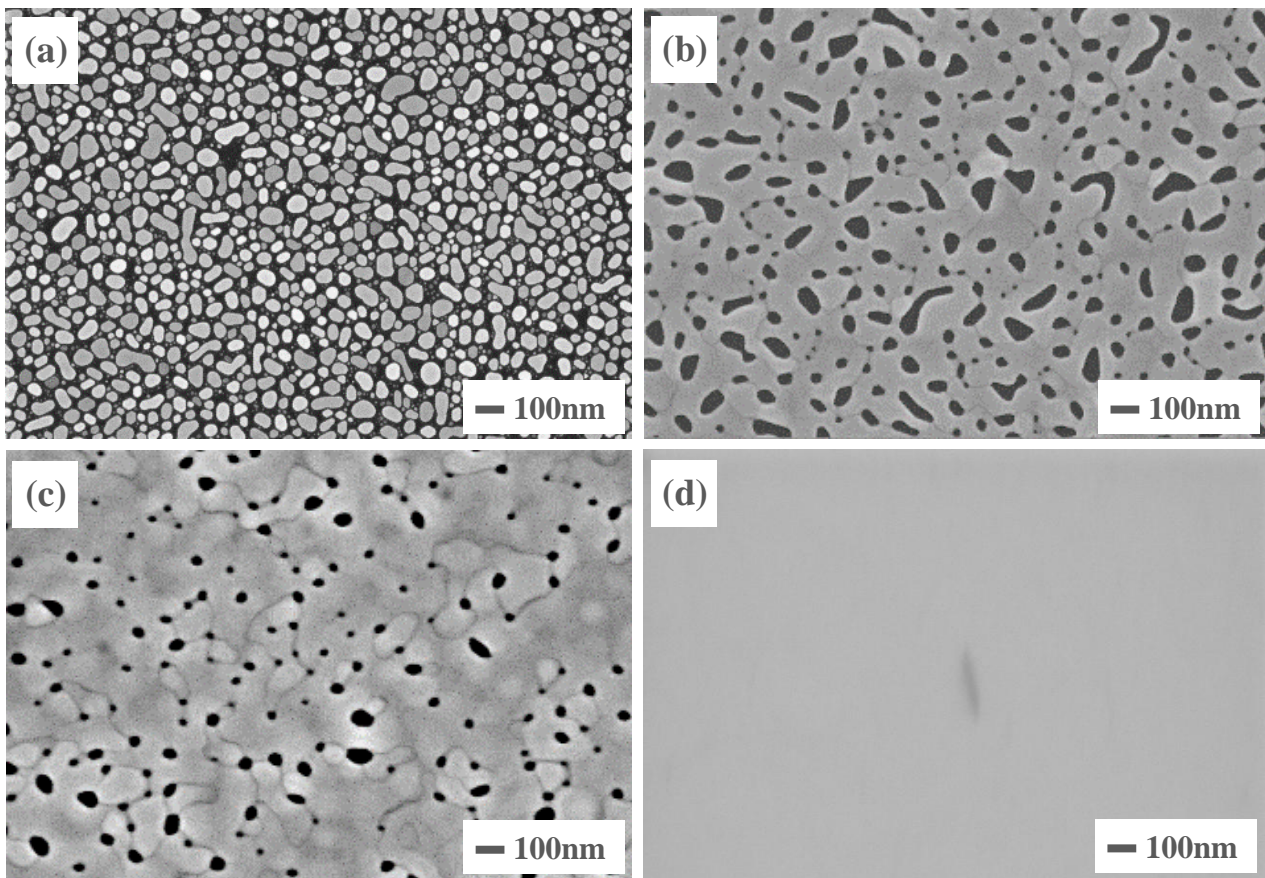


**Figure 3.** SEM images of SCULL silver film growth in the second step from AFT 2D island seeds to a continuous film. (a) Initial AFT 2D Ag(111) islands. Additional evaporation of silver [(b) 10-nm and (c) 20-nm thickness] on AFT 2D seeds at room temperature. (d) A 35-nm-thick single-crystalline silver annealed film. The defect on the film surface was purposefully created to facilitate focusing on the surface of the atomically flat film.

The optimization of the second step parameters enables the spreading of Ag(111) 2D islands, in a manner similar to a solid phase epitaxy process, toward a fully continuous film but under less demanding vacuum conditions. Upon subsequent annealing at temperatures from 320-480 °C, the silver film's crystalline structure and surface roughness are improved, along with a reduction in the defect density. We assume that rapid thermal annealing can be used for the final annealing step, which further reduces the total processing time. Using the SCULL process, the well-known problem of substrate surface silver dewetting under elevated temperatures for sub-50 nm single-crystalline silver film deposition is solved. The growth of a continuous silver film is demonstrated with a thickness down to 12 nm.

The microstructure of the samples on silicon substrates was analyzed using high-resolution wide-angle X-ray diffraction (XRD) (see the Supporting Information for details). The X-ray out-of-plane diffraction pattern (**Figure 4a**) and phi-scan pattern (Figure 4c) show, that the sample S1 is a biaxially textured silver film on a single-crystalline silicon substrate. Epitaxial relationship is (111)Ag//(111)Si:[111]Ag//[111]Si. The average lattice parameter for all measured samples is  $4.076 \pm 0.004 \text{ \AA}$ , which is in good agreement with the known value for the atomic weight of pure Ag.<sup>[34]</sup> Additionally, the  $\phi$ -scans (Figure 4c) show that the misorientation of the film and substrate is less than  $0.1^\circ$ . The rocking curve (Figure 4b) through the Ag(111) peak has a full-width-at-half-maximum (FWHM) of  $0.325^\circ$ . Fitting of the X-ray reflection curve (Figure 4d) with a 2-layer model (Ag/Si) suggest that the S1 silver surface roughness is approximately 0.7 nm, which is in good agreement with the atomic force microscopy (AFM) measured value. The FWHM value for the S1 sample was comparable to that of previously reported single-crystalline silver films of greater thicknesses:  $0.116^\circ$  for a 1- $\mu\text{m}$ -thick Ag film<sup>[35]</sup> and  $0.22^\circ$  for a 200-nm-thick Ag film.<sup>[14]</sup>

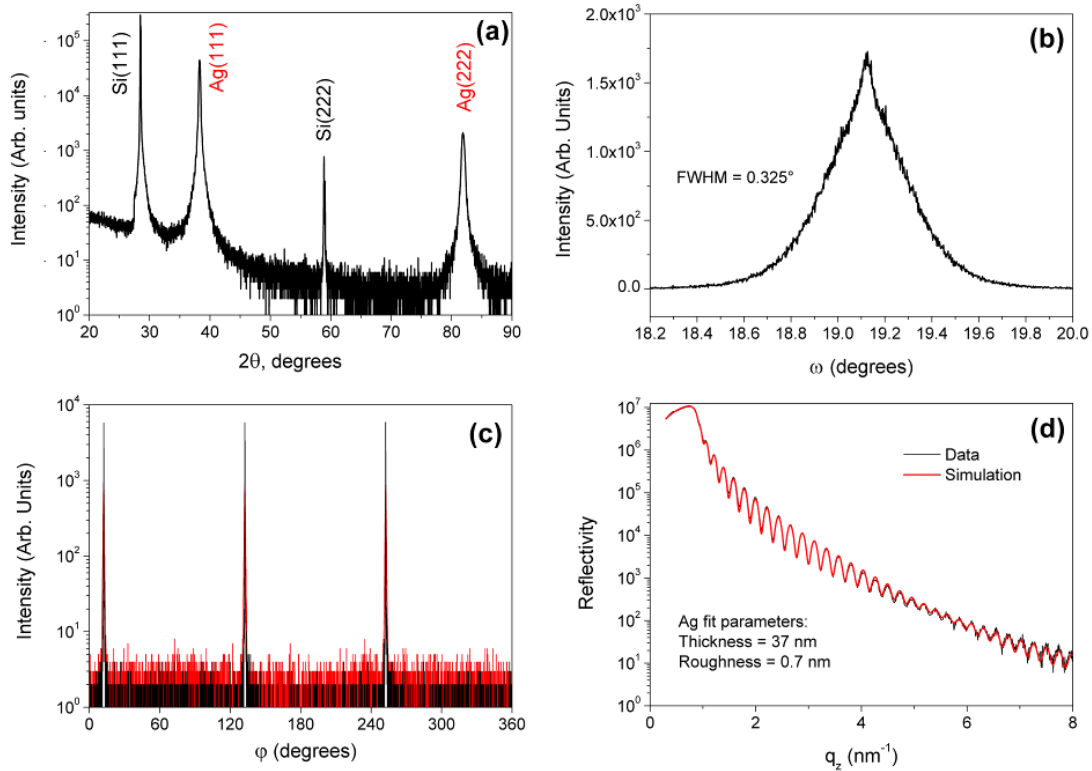


**Figure 4.** XRD characterization of a 35-nm-thick Si(111)/Ag(111) film (S1). (a) High-resolution X-ray diffraction ( $\theta$ - $2\theta$ ) pattern. (b) Measured transverse scan (rocking curve,  $\omega$ -scan) through the Ag(111) diffraction peak. (c) Grazing incidence of the in-plane X-ray diffraction scan ( $\phi$ -scans) of the Ag(111) plane. (d) X-ray reflectivity curve.

The surface morphology of the as-fabricated films was characterized by a stylus profilometer (SP) and by AFM within one week after deposition. Low-noise, high-quality SP surface roughness scans over a 20- $\mu\text{m}$  length were used as quick and reliable feedback for the technology development. The surface of the films was continuous without pinholes, and no grain boundaries were found (**Figure 5**). The S1 films were extremely smooth with a root mean square (RMS) AFM roughness of 0.09 nm (Figure 5a), as measured over a  $2.5 \times 2.5 \mu\text{m}^2$ . The RMS SP roughness was 0.71 nm, which is close to the value of 0.46 nm extracted from the X-ray reflectivity and close to the AFM roughness value of 0.52 nm (Figure 5b), measured over a  $50 \times 50 \mu\text{m}^2$  area. Global initial substrate nonflatness could be observed (Figure 5b). The RMS AFM roughness values of thicker films on silicon S7 and films on mica M1 are slightly larger, but still very good 0.43 nm (Figure 5c) and 0.35 nm (Figure

5d), respectively. The stacking growth of the epitaxial monolayers is observed for sample S7, which can be improved by the SCULL process in the last stage optimization.

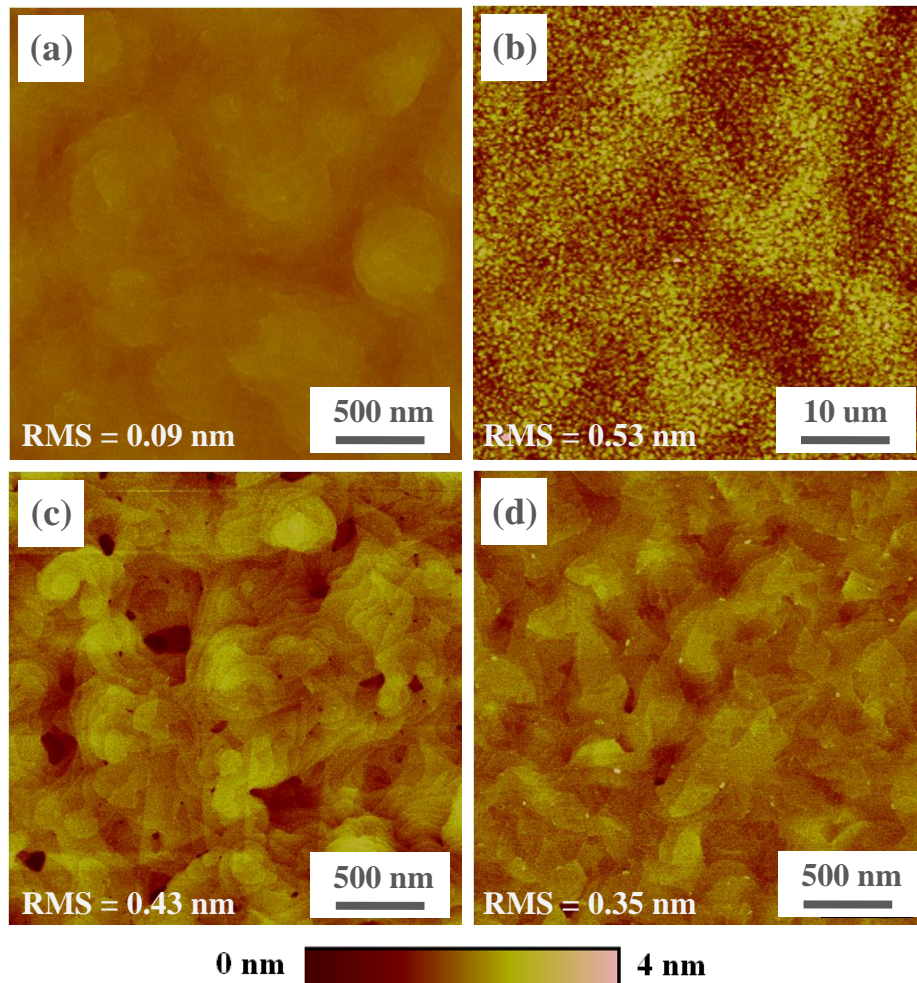


**Figure 5.** AFM scans of single-crystalline silver films S1 (a), S7 (c) and M1 (d) measured over a  $2.5 \times 2.5 \mu\text{m}^2$  area, and silver films S1 (b) measured over a  $50 \times 50 \mu\text{m}^2$  area. The RMS roughness of these films is 0.09, 0.43, 0.35 and 0.52 nm, respectively.

To determine the optical parameters of the films, multi-angle spectroscopic ellipsometry was used (at three angles of incidence:  $50^\circ$ ,  $60^\circ$  and  $70^\circ$ ). The film thickness was precisely estimated before ellipsometry modeling using SP step height measurements, scanning electron microscopy (SEM) of the cross section (after cleaving), XRD and SEM/energy-dispersive X-ray (EDX) thickness extraction. To characterize the optical losses, the real and imaginary parts of the dielectric permittivity were calculated based on the measured ellipsometric parameters ( $\Psi$  and  $\Delta$ ). Dielectric

permittivity data were compared (**Figure 6**) with those reported by Johnson and Christy (JC), which they averaged from measurements of two silver films with a thickness of 30.4 and 37.5 nm.<sup>[11]</sup> S1 had an imaginary part (related to optical losses) of the dielectric permittivity ( $\epsilon''$ ) of less than 0.1 in the 370-600 nm wavelength range and less than 0.3 in the 350-850 nm wavelength range. At the same moment, the real part of the dielectric permittivity ( $\epsilon'$ ) tended to increase (in absolute value) with the wavelength compared to the JC data, indicating a higher conductivity of the films.<sup>[14]</sup>

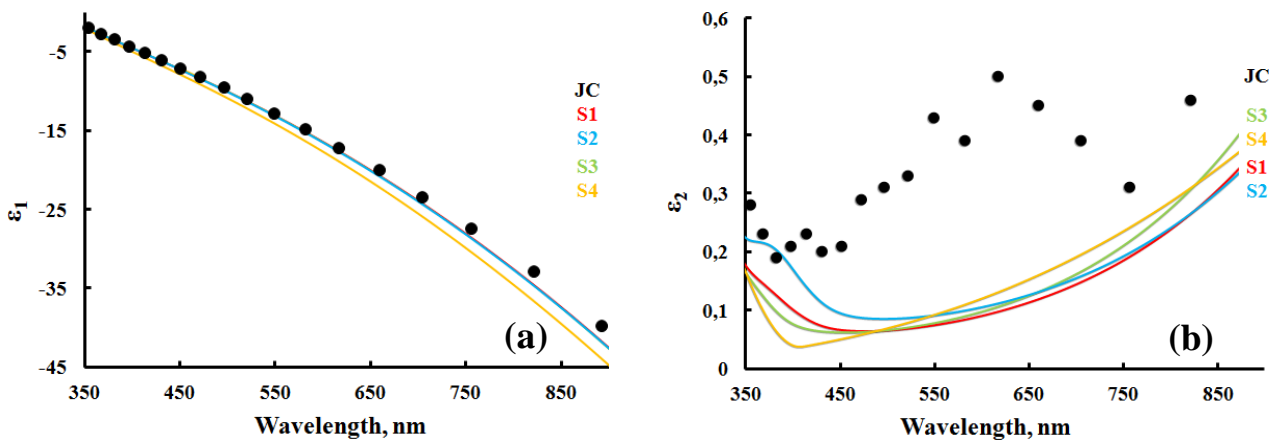


**Figure 6.** Real (a) and imaginary (b) parts of the dielectric permittivity of the single-crystalline silver films. Ellipsometric data were acquired over the 350-900 nm wavelength range. Three different incidence angles were used: 50, 60, and 70°. The dielectric functions were fitted using the Brendel oscillator model. JC – dielectric permittivity reported by Johnson and Christy.<sup>[11]</sup>

In this paper, the SCULL process is demonstrated for a continuous 35 to 100-nm-thick atomically-flat single-crystalline silver film deposition over a standard chip area ( $15 \times 15 \text{ mm}^2$ ). The films could be reproducibly fabricated in a few hours using a high vacuum e-beam evaporator, which is installed in most standard cleanrooms. The excellent physical and optical properties of SCULL single-crystalline films may offer the potential for a variety of extended practical applications in nanophotonics,<sup>[4,5]</sup> plasmonics,<sup>[3]</sup> and biophotonics.<sup>[6]</sup> Ultrabright room-temperature single-photon quantum emitters could be imagined, and they have recently opened fundamentally new possibilities in quantum information and sensing applications. Nowadays, the typical detected

photon rates from quantum emitters range from  $10^4$  to  $10^5$  counts per second (cps),<sup>[26]</sup> and they occasionally exceed  $10^6$  cps.<sup>[36]</sup> Using SCULL Ag films, the all-silver ultrabright room-temperature single-photon quantum emitters were demonstrated with detected photon rates reaching 50 million cps,<sup>[37]</sup> which is the highest rate ever observed in room-temperature quantum emitters and orders of magnitude higher than the polycrystalline silver emitter.<sup>[37]</sup> The SCULL process has been approved for silver, gold and aluminum film evaporation, and it could be used for the deposition of a variety of extremely flat sub-100 nm single-crystalline metal films. The SCULL process could be easily integrated and is completely compatible with mass production top-down semiconductor techniques.

### **Supporting Information**

Supporting Information is available from the Wiley Online Library or from the author.

### **Acknowledgements**

The SCULL metal growth process was developed by Ilya A. Rodionov, Ilya A. Ryzhikov, and Aleksandr S. Baburin. We would like to thank Vladimir M. Shalaev, Alexandra Boltasseva, Denis A. Fokin, Alexander M. Merzlikin, Alexander V. Baryshev and Alexander S. Dorofeenko for the helpful discussions. The SCULL process was developed and the samples were prepared at the BMSTU Nanofabrication Facility (Functional Micro/Nanosystems, FMNS REC, ID 74300).

Received: ((will be filled in by the editorial staff))

Revised: ((will be filled in by the editorial staff))

Published online: ((will be filled in by the editorial staff))

## References

- [1] A. Melikyan, L. Alloatti, A. Muslija, D. Hillerkuss, P. C. Schindler, J. Li, R. Palmer, D. Korn, S. Muehlbrandt, D. Van Thourhout, B. Chen, R. Dinu, M. Sommer, C. Koos, M. Kohl, W. Freude, J. Leuthold, *Nat. Photonics* **2014**, *8*, 229.
- [2] S. I. Bozhevolnyi, V. S. Volkov, E. Devaux, J.-Y. Laluet, T. W. Ebbesen, *Nature* **2006**, *440*, 508.
- [3] P. Melentiev, A. Kalmykov, A. Gritchenko, A. Afanasiev, V. Balykin, A. S. Baburin, E. Ryzhova, I. Filippov, I. A. Rodionov, I. A. Nechepurenko, A. V. Dorofeenko, I. Ryzhikov, A. P. Vinogradov, A. A. Zyablovsky, E. S. Andrianov, A. A. Lisyansky, *Appl. Phys. Lett.* **2017**, *111*, 213104.
- [4] R. F. Oulton, V. J. Sorger, T. Zentgraf, R.-M. Ma, C. Gladden, L. Dai, G. Bartal, X. Zhang, *Nature* **2009**, *461*, 629.
- [5] Y. J. Lu, J. Kim, H. Y. Chen, C. Wu, N. Dabidian, C. E. Sanders, C. Y. Wang, M. Y. Lu, B. H. Li, X. Qiu, W. H. Chang, L. J. Chen, G. Shvets, C. K. Shih, S. Gwo, *Science* **2012**, *337*, 450.
- [6] J. N. Anker, W. P. Hall, O. Lyandres, N. C. Shah, J. Zhao, R. P. Van Duyne, *Nat. Mater.* **2008**, *7*, 442.
- [7] A. L. Pyayt, B. Wiley, Y. Xia, A. Chen, L. Dalton, *Nat. Nanotechnol.* **2008**, *3*, 660.
- [8] H. A. Atwater, A. Polman, *Nat. Mater.* **2010**, *9*, 205.
- [9] A. C. Atre, A. García - Etxarri, H. Alaeian, J. A. Dionne, *Adv. Opt. Mater.* **2013**, *1*, 327.
- [10] A. Boltasseva, H. A. Atwater, *Science* **2011**, *331*, 290.
- [11] P. B. Johnson, R. W. Christy, *Phys. Rev. B* **1972**, *6*, 4370.
- [12] P. R. West, S. Ishii, G. V. Naik, N. K. Emani, V. M. Shalaev, A. Boltasseva, *Laser Photonics Rev.* **2010**, *4*, 795.
- [13] B. Dastmalchi, P. Tassin, T. Koschny, C. M. Soukoulis, *Adv. Opt. Mater.* **2016**, *4*, 177.
- [14] J. H. Park, P. Ambwani, M. Manno, N. C. Lindquist, P. Nagpal, S.-H. Oh, C. Leighton, D. J. Norris, *Adv. Mater.* **2012**, *24*, 3988.

- [15] Y. Wu, C. Zhang, N. M. Estakhri, Y. Zhao, J. Kim, M. Zhang, X.-X. Liu, G. K. Pribil, A. Alù, C.-K. Shih, X. Li, *Adv. Mater.* **2014**, *26*, 6106.
- [16] R. Malureanu, A. Lavrinenko, *Nanotechnol. Rev.* **2015**, *4*, 259.
- [17] K. M. McPeak, S. V. Jayanti, S. J. P. Kress, S. Meyer, S. Iotti, A. Rossinelli, D. J. Norris, *ACS Photonics* **2015**, *2*, 326.
- [18] S. Kunwar, M. Sui, Q. Zhang, P. Pandey, M.-Y. Li, J. Lee, *Nano-Micro Lett.* **2017**, *9*, 17.
- [19] A. R. Smith, K. J. Chao, Q. Niu, C. K. Shih, *Science* **1996**, *273*, 226.
- [20] T. Hanawa, K. Oura, *Jpn. J. Appl. Phys.* **1977**, *16*, 519.
- [21] A. S. Baburin, A. R. Gabidullin, A. V. Zverev, I. A. Rodionov, I. A. Ryzhikov, Y. V. Panfilov, *Vestn. Mosk. Gos. Tekh. Univ. im. N.E. Bauman, Priborostr.* **2016**, *6*, 4.
- [22] I. A. Rodionov, A. S. Baburin, A. V. Zverev, I. A. Philippov, A. R. Gabidulin, A. A. Dobronosova, E. V. Ryzhova, A. P. Vinogradov, A. I. Ivanov, S. S. Maklakov, *Proc. SPIE* **2017**, *10343*, 1034337.
- [23] N. N. Durmanov, R. R. Guliev, A. V. Eremenko, I. A. Boginskaya, I. A. Ryzhikov, E. A. Trifonova, E. V. Putlyayev, A. N. Mukhin, S. L. Kalnov, M. V. Balandina, A. P. Tkachuk, V. A. Gushchin, A. K. Sarychev, A. N. Lagarkov, I. A. Rodionov, A. R. Gabidullin, I. N. Kurochkin, *Sens. Actuators, B* **2018**, *257*, 37.
- [24] A. A. Baski, H. Fuchs, *Surf. Sci.* **1994**, *313*, 275.
- [25] R. Kern, G. Metois, *Curr. Top. Mater. Sci.* **1979**, *3*, 131.
- [26] D. K. Goswami, K. Bhattacharjee, B. Satpati, S. Roy, P. V. Satyam, B. N. Dev, *Surf. Sci.* **2007**, *601*, 603.
- [27] D. A. Fokin, S. I. Bozhko, V. Dubost, F. Debontridder, A. M. Ionov, T. Cren, D. Roditchev, *Phys. Status Solidi* **2010**, *7*, 165.
- [28] Z. H. Zhang, S. Hasegawa, S. Ino, *Phys. Rev. B* **1997**, *55*, 9983.
- [29] W. B. Su, S. H. Chang, W. B. Jian, C. S. Chang, L. J. Chen, T. T. Tsong, *Phys. Rev. Lett.* **2001**, *86*, 5116.

- [30] P. Czoschke, H. Hong, L. Basile, T.-C. Chiang, *Phys. Rev. B* **2005**, 72, 075402.
- [31] K. Bromann, H. Brune, H. Röder, K. Kern, *Phys. Rev. Lett.* **1995**, 75, 677.
- [32] I. B. Altfeder, K. A. Matveev, D. M. Chen, *Phys. Rev. Lett.* **1997**, 78, 2815.
- [33] F. Sette, T. Hashizume, F. Comin, A. A. MacDowell, P. H. Citrin, *Phys. Rev. Lett.* **1988**, 61, 1384.
- [34] W. P. Davey, *Phys. Rev.* **1925**, 25, 753.
- [35] A. A. High, R. C. Devlin, A. Dibos, M. Polking, D. S. Wild, J. Perczel, N. P. de Leon, M. D. Lukin, H. Park, *Nature* **2015**, 522, 192.
- [36] T. T. Tran, K. Bray, M. J. Ford, M. Toth, I. Aharonovich, *Nat. Nanotechnol.* **2015**, 11, 37.
- [37] S. Bogdanov, M. Y. Shalaginov, A. Lagutchev, C.-C. Chiang, D. Shah, A. S. Baburin, I. A. Ryzhikov, I. A. Rodionov, A. Boltasseva, V. M. Shalaev, *arXiv:1711.09481* **2017**.

## Supporting Information

### **Synthesis of Low-loss Single-crystalline Silver Films for Quantum Nanophotonics**

*Ilya A. Rodionov\**, Aleksandr S. Baburin, Alexey P. Vinogradov, Aidar R. Gabidullin, Sergey S.

*Maklakov, Swen Peters, Ilya A. Ryzhikov, and Alexander V. Andriyash*

## 1. Experimental Section

### 1.1. Preparation of Epitaxial Films

Epitaxial films of silver were deposited on silicon (100), (110), (111) and muscovite mica substrates using 10 kW e-beam evaporator (Angstrom Engineering) with a base pressure lower than  $3 \times 10^{-8}$  Torr. Mica substrates were cleaved perpendicular to the c-axis to reveal fresh surfaces, prior to deposition. All films were grown using 5N (99.999%) pure silver. Films were deposited with rate of  $0.5\text{-}10 \text{ \AA s}^{-1}$  measured with quartz monitor at approximate source to substrate distance of 30 cm. Deposition is done in two steps using SCULL process. First, seed island layer is deposited on the elevated temperature substrate. At the second step evaporation is stopped and the substrate is cooled to room temperature. Then, silver deposit is started on seed layer until continuous single-crystalline film is formed. Different temperature in a range from room temperature to  $450^\circ\text{C}$  were used.

## 2. Ag Films Characterization

### 2.1. X-Ray Diffraction (XRD)

X-ray diffraction was studied by means of the Rigaku SmartLab diffractometer. Parallel beam geometry and Cu  $K\alpha 1$  radiation was applied. X-ray diffraction pattern was measured in  $2\theta/\omega$  mode from  $20^\circ$  to  $90^\circ$  ( $2\theta$ ) with  $0.02^\circ$  step. To study texture and azimuthal orientation of silver crystals in relation to silicon monocrystal axes,  $\phi$ -scans for both Ag and Si layers were measured from  $0^\circ$  to  $360^\circ$  with  $0.052^\circ$  step. Rocking curves (or  $\omega$ -scans,  $0.001^\circ$  step) were applied to characterize in-plane perfection of silver crystals. Position of X-ray reflections and full width at half maximum values of the rocking curves were determined through experimental data approximation with a pseudo-Voigt function by means of a CSD software package.<sup>[S1]</sup>

In each sample, observed reflections were caused by sets of crystallographic planes with divisible Miller indices. This means that crystallographic planes of silver crystals were parallel to planes of the substrate with the same Miller indices. Ag(111) was parallel to Si(111), Ag(110)//Si(110) and Ag(100)//Si(100). A difference in value of lattice parameter of silver on substrate with various Si orientations, if any, was lower than uncertainty of the method of investigation. Averaged out of all

samples lattice parameter was  $4.076 \pm 0.004 \text{ \AA}$ , which was in good agreement with known value for pure Ag atomic weight.<sup>[S2]</sup> Curves of  $\varphi$ -scans consisted of sharp reflections for all the samples (**Figure S1**). The number and position of these reflections coincided with standard (111), (110) and (001) FCC crystal projections. Also, the position of reflections from the silver film matched in each case to a position of those of a silicon substrate. This result meant that each studied silver film possessed biaxial texture. Analysis of  $2\theta/\omega$  and  $\varphi$ -scans showed that each studied sample was biaxially textured silver film on mono-crystalline silicon substrate with the following epitaxial relationships: (111)Ag//(111)Si:[111]Ag//[111]Si, (110)Ag//(110)Si:[110]Ag//[110]Si and (001)Ag//(001)Si:[001]Ag//[001]Si. Additionally,  $\varphi$ -scans showed that misorientation of these films and a substrate did not exceed  $0.1^\circ$ . Appearance of a Si(222) forbidden reflection is in accordance with recently published investigations.<sup>[S3]</sup>

Since full-width-at-half-maximum (FWHM) of a rocking curve profile serves as a practical numerical characteristic of mosaic spread<sup>[S2]</sup> in thin crystalline films for plasmonics,<sup>[S4]</sup> precise determination of this value is of importance. The values derived were:  $0.325^\circ$  for S1 sample,  $0.829^\circ$  for S2 and  $0.831^\circ$  for S3. The FWHM value for S1 sample was comparable to that of a previously reported single-crystalline films for modern plasmonic applications but of larger thicknesses:  $0.116^\circ$  for  $1\text{-}\mu\text{m}$  thick Ag film<sup>[S5]</sup> and  $0.22^\circ$  for  $200\text{-nm}$  thick Ag film.<sup>[S6]</sup> S7 sample showed same diffractometric character as S1 and a rocking curve FWHM value of  $0.368^\circ$ .

## 2.2. Atomic Force Microscopy (AFM)

The atomic force microscope Bruker Dimension Icon with SCANASYST-AIR-HR probe (with nominal tip radius of  $2 \text{ nm}$ ) was used. All AFM images were obtained by using PeakForce Tapping mode with ScanAsyst imaging and the scanned area was  $2.5 \times 2.5 \text{ }\mu\text{m}^2$  and  $50 \times 50 \text{ }\mu\text{m}^2$ . Nanoscope software was utilized to analyze the images and extract root mean square roughness.

## 2.3. Ellipsometry

Dielectric functions of the silver films were measured using a multi-angle spectroscopic ellipsometer Sentech SER 800. The models were developed in cooperation with Sentech GmbH

application department. Measurement spectral wavelength range was from 380 to 1000 nm, with an interval of 1 nm, and the reflected light was analyzed at incidence angles of 50°, 60°, 70°. By using SENresearch 4.0 software. The dielectric functions were fitted with Brendel model. A two layer model (air and Ag) with a perfectly flat interface was assumed. For all samples, the mean square errors, representing the quality of the match between the measured and theoretically calculated dielectric functions, were less than 0.3°, which implies good consistency between them.

#### **2.4. Profilometry**

The stylus profiler KLA Tencor P17 was used. Durasharp stylus with 38 nm tip radius was used. All measurements were done by using 0.5 mg tapping strength, scan rate was 2  $\mu\text{m s}^{-1}$  and the scanned line length was 20  $\mu\text{m}$ .

#### **2.5. Scanning Electron Microscopy**

In order to check the quality and uniformity of the deposited layers silver films surfaces after deposition were investigated by means of scanning electron microscope Zeiss Merlin with Gemini II column. All SEM images were obtained using in-lens detector and the accelerating voltage 5 kV and working distance from the sample to detector from 1 to 4 mm. Magnifications 3000, 7000, 15000 and 50000 were used to fully analyze samples.

## Supporting Information References

- [S1] L. Akselrud, Y. Grin, *J. Appl. Crystallogr.* **2014**, *47*, 803.
- [S2] W. P. Davey, *Phys. Rev.* **1925**, *25*, 753.
- [S3] P. Zaumseil, *J. Appl. Crystallogr.* **2015**, *48(Pt 2)*, 528.
- [S4] O. Durand, A. Letoublon, D. J. Rogers, F. H. Teherani, *Thin Solid Films* **2011**, *519*, 6369.
- [S5] A. A. High, R. C. Devlin, A. Dibos, M. Polking, D. S. Wild, J. Perczel, N. P. de Leon, M. D. Lukin, H. Park, *Nature* **2015**, *522*, 192.
- [S6] J. H. Park, P. Ambwani, M. Manno, N. C. Lindquist, P. Nagpal, S.-H. Oh, C. Leighton, D. J. Norris, *Adv. Mater.* **2012**, *24*, 3988.

## Supplemental Figures

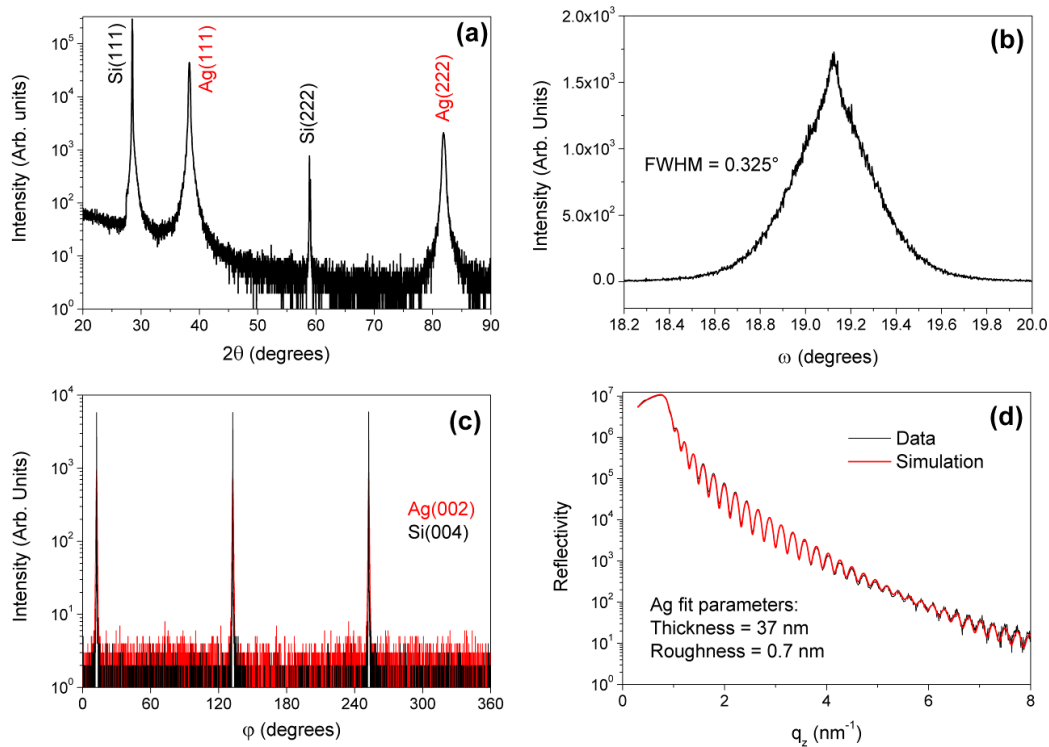


**Figure S1.** XRD characterization of a nominally 35-nm-thick Si(111)/Ag(111) film (S1). (a) High-resolution X-ray diffraction ( $\theta$ - $2\theta$ ) pattern. (b) Measured transverse scan (rocking curve,  $\omega$ -scan) through the Ag(111) diffraction peak. (c) Grazing incidence of the in-plane X-ray diffraction scan ( $\phi$ -scans) of the Ag(111) plane. (d) X-ray reflectivity curve.

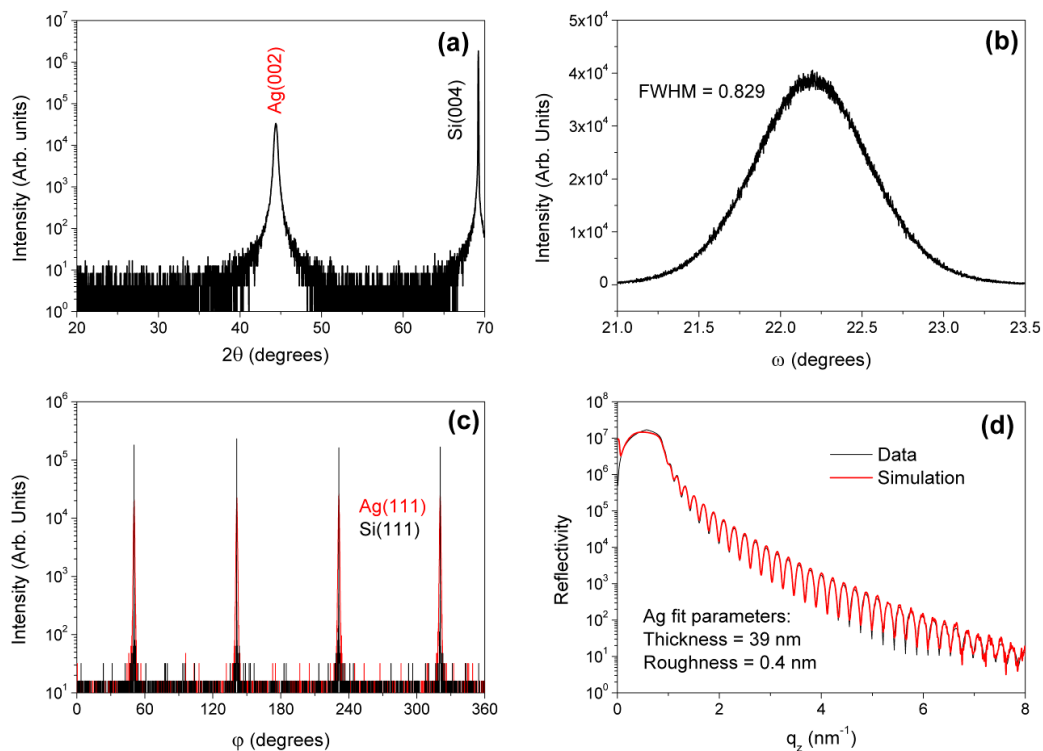


**Figure S2.** XRD characterization of a nominally 35-nm-thick Si(111)/Ag(111) film (S2). (a) High-resolution X-ray diffraction ( $\theta$ - $2\theta$ ) pattern. (b) Measured transverse scan (rocking curve,  $\omega$ -scan) through the Ag(111) diffraction peak. (c) Grazing incidence of the in-plane X-ray diffraction scan (phi-scans) of the Ag(111) plane. (d) X-ray reflectivity curve.

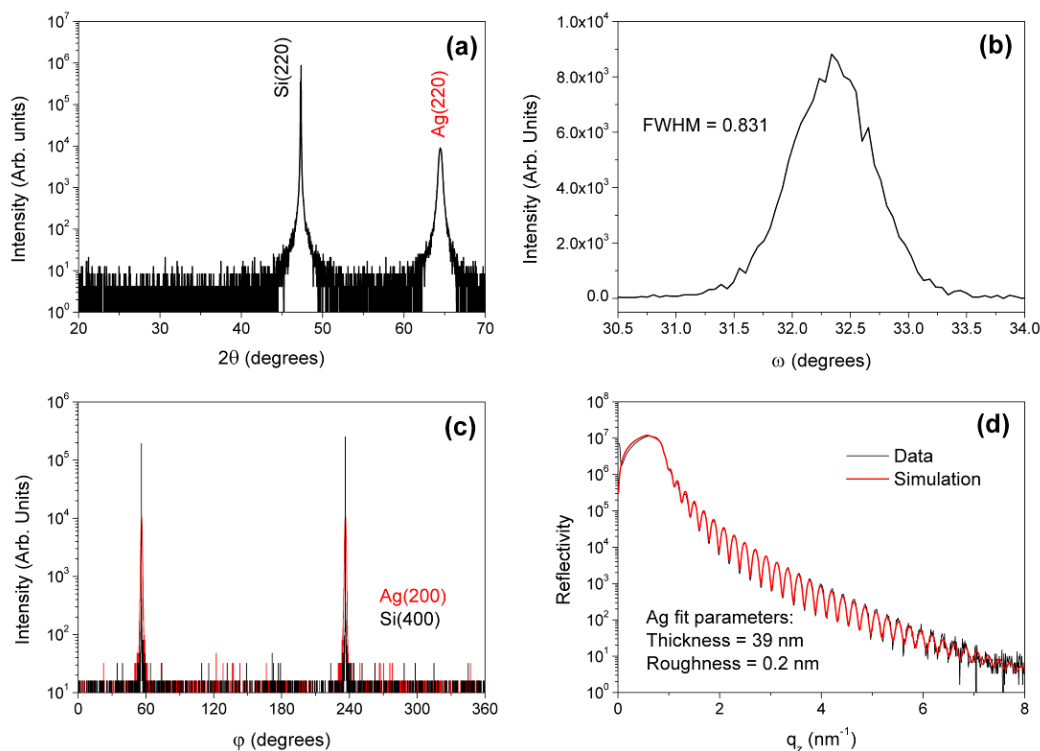


**Figure S3.** XRD characterization of a nominally 35-nm-thick Si(111)/Ag(111) film (S3). (a) High-resolution X-ray diffraction ( $\theta$ - $2\theta$ ) pattern. (b) Measured transverse scan (rocking curve,  $\omega$ -scan) through the Ag(111) diffraction peak. (c) Grazing incidence of the in-plane X-ray diffraction scan (phi-scans) of the Ag(111) plane. (d) X-ray reflectivity curve.

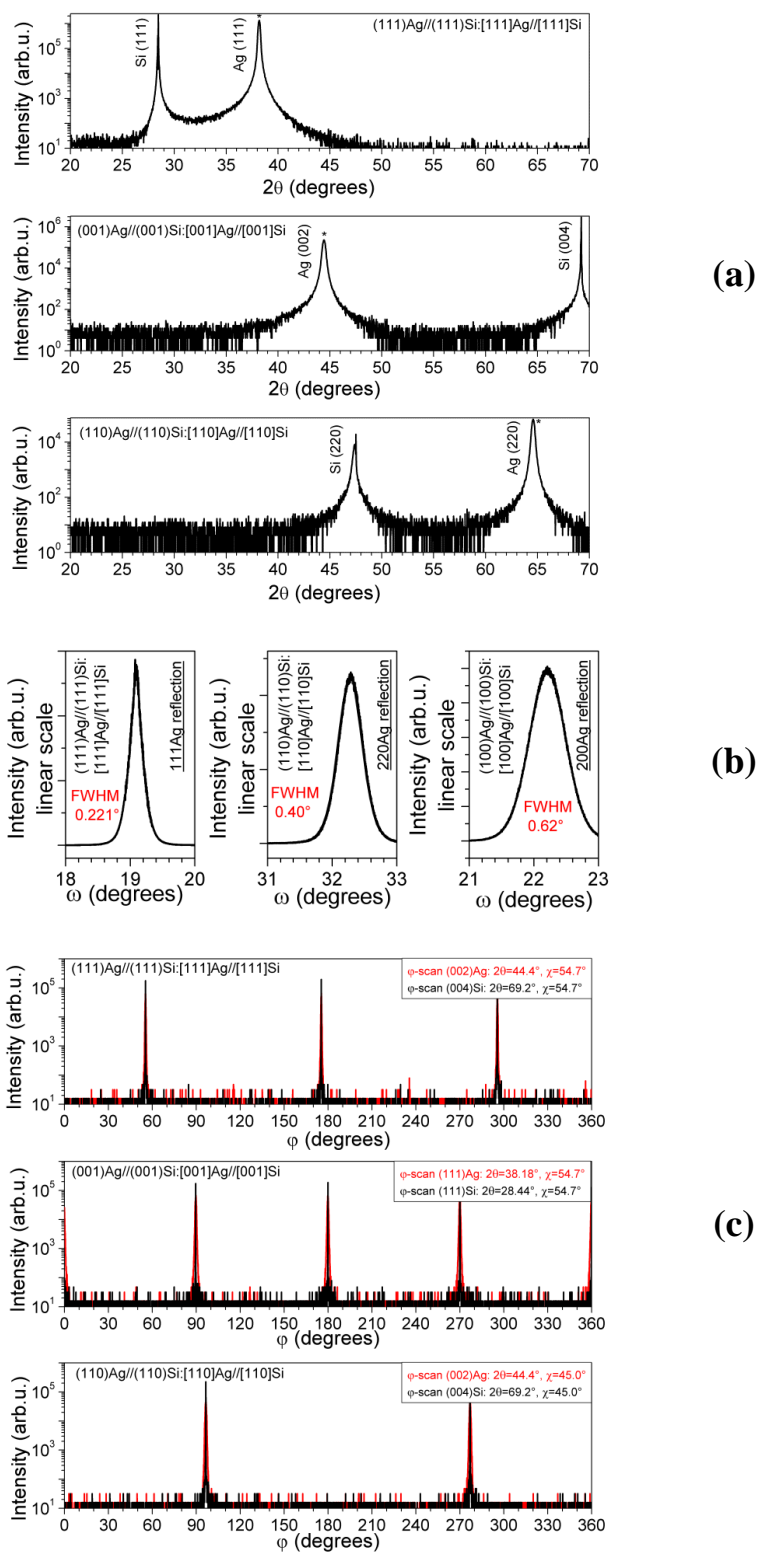


**Figure S4.** XRD characterization of a nominally 65-nm-thick Ag films S4-S6. (a) High-resolution X-ray diffraction ( $\theta$ - $2\theta$ ) pattern. (b) Measured transverse scan (rocking curve,  $\omega$ -scan) through the Ag diffraction peak. (c) Grazing incidence of the in-plane X-ray diffraction scan (phi-scans) of the Ag plane.

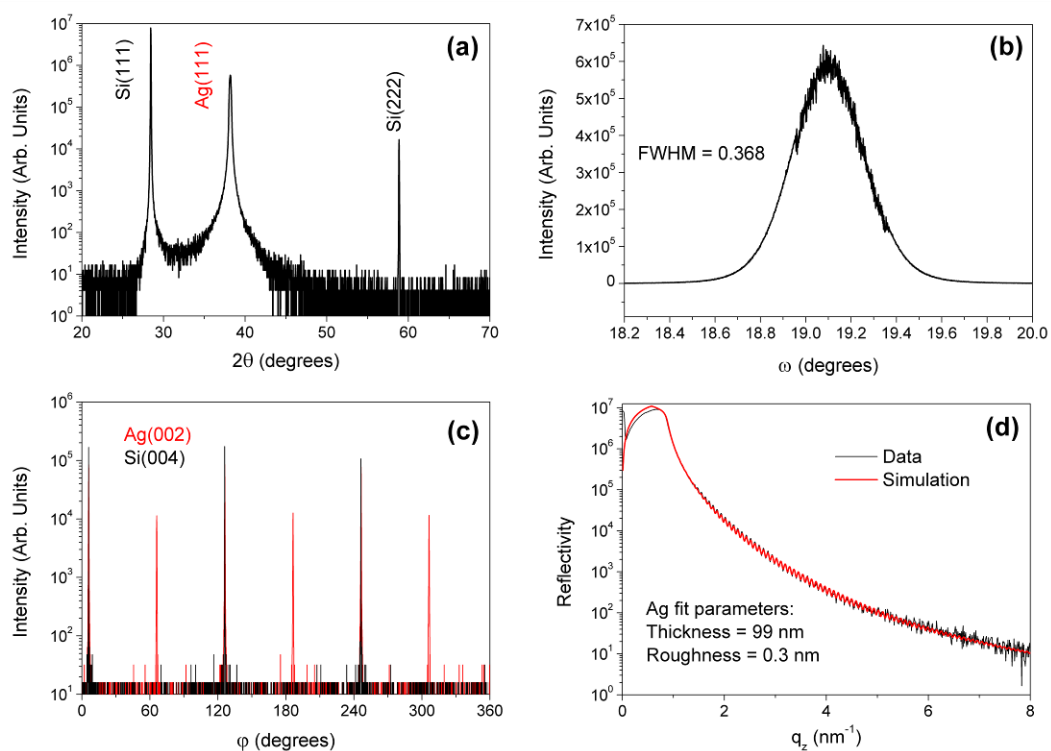


**Figure S5.** XRD characterization of a nominally 100-nm-thick Si(111)/Ag(111) film (S7). (a) High-resolution X-ray diffraction ( $\theta$ - $2\theta$ ) pattern. (b) Measured transverse scan (rocking curve,  $\omega$ -scan) through the Ag(111) diffraction peak. (c) Grazing incidence of the in-plane X-ray diffraction scan ( $\phi$ -scans) of the Ag(111) plane. (d) X-ray reflectivity curve.